141 (2022) 213097

Contents lists available at ScienceDirect

Biomaterials Advances

journal homepage: www.journals.elsevier.com/materials-science-and-engineering-c

Bactericidal activity of $Ag_4V_2O_7/\beta$-$AgVO_3$ heterostructures against antibiotic-resistant *Klebsiella pneumoniae*

Marcelo Assis [a,b,c,*], Jussara Soares da Silva [b,1], Mariana Ottaiano Gonçalves [d], Joice Margareth de Almeida Rodolpho [e], Bruna Dias de Lima Fragelli [e], Ana Beatriz Pereira Corte [b], Lara Kelly Ribeiro [a,b], Marcio Daldin Teodoro [f], Fernanda de Freitas Anibal [e], Cristina Paiva de Sousa [d], Osvaldo N. Oliveira Jr [c], Juan Andrés [a], Elson Longo [b]

[a] Department of Analytical and Physical Chemistry, University Jaume I (UJI), 12071 Castelló, Spain
[b] CDMF, LIEC, Federal University of São Carlos (UFSCar), 13565-905 São Carlos, SP, Brazil
[c] São Carlos Institute of Physics, University of São Paulo (USP), 13560-970 São Carlos, SP, Brazil
[d] LaMiB, Federal University of São Carlos (UFSCar), 13565-905 São Carlos, SP, Brazil
[e] Laboratory of Inflammation and Infectious Diseases, Department of Morphology and Pathology, Federal University of São Carlos (UFSCar), 13565-905 São Carlos, SP, Brazil
[f] Physics Department, Federal University of São Carlos (UFSCar), 13565-905 São Carlos, SP, Brazil

ARTICLE INFO

Keywords:
$Ag_4V_2O_7$
β-$AgVO_3$
Semiconductor heterostructures
Antimicrobial activity
Cytotoxicity
Phytotoxicity

ABSTRACT

Although Ag-based materials are efficient against antibiotic-resistant bacteria, their high toxicity to living organisms represents a major challenge for obtaining useful products. In this work, we report the bactericidal activity of $Ag_4V_2O_7/\beta$-$AgVO_3$ heterostructures, which proved to be effective against *Klebsiella pneumoniae* (ATCC 1706, a standard strain; A54970, a multidrug-resistant carbapenemase (KPC)-producing strain; A34057, a multidrug-resistant strain capable of producing extended spectrum beta-lactamases (ESBL); and a community-isolated strain, A58240) at minimum inhibitory concentrations (MIC) as low as 62.5 μg/mL. This activity is higher than that reported for the individual silver vanadates ($Ag_4V_2O_7$ or β-$AgVO_3$) owing to the synergistic interactions between both semiconductors. However, the most efficient heterostructure was found to be toxic to mouse 3 T3 fibroblasts and to L. *sativa* and *C. sativus* seeds, as indicated by MTT ((4,5 - dimethylthiazol -2yl) 2,5 -diphenylbromide), neutral red assays and germination index measurements. The antimicrobial, phytotoxic and cytotoxic activities were all associated with an efficient generation of reactive oxygen species (ROS) in the heterostructure, especially •OH and $\bullet O_2^-$ radicals. The ROS production by $Ag_4V_2O_7/\beta$-$AgVO_3$ heterostructures was measured through photodegradation studies with Rhodamine B. While the bactericidal activity of the heterostructures is promising, especially when compared to Ag-based materials, their use in practical applications will require encapsulation either to avoid leaching or to mitigate their toxicity to humans, animals and plants.

1. Introduction

Antibiotic-resistant bacteria are a severe public health problem according to the World Health Organization (WHO). For such reason, in order to reduce the spread of antimicrobial resistance and help in the prevention of infections, the WHO published in 2017 a list of 12 classes of bacteria resistant to most existing treatments [1,2], including the Gram-negative bacterium *Klebsiella pneumoniae* (*K. pneumoniae*) – an opportunistic pathogen that can cause various infections and that is increasingly resistant to antibiotics [3,4]. Thus, it becomes extremely necessary not only to develop effective drugs to combat bacteria, but also to design some strategies to prevent new infections. The latter includes surface coatings to eliminate microorganisms by contact, or the use of polymer additives to prevent bacteria proliferation [5–8]. Silver-based materials are considered promising candidates for antimicrobial agents due to their ability to produce reactive oxygen species (ROS) even

* Corresponding author at: Department of Analytical and Physical Chemistry, University Jaume I (UJI), 12071 Castelló, Spain.
E-mail address: marcelostassis@gmail.com (M. Assis).
[1] The authors contributed equally to the work.

https://doi.org/10.1016/j.bioadv.2022.213097
Received 18 May 2022; Received in revised form 26 July 2022; Accepted 24 August 2022
Available online 31 August 2022

in dark conditions, in addition to their possible controlled release of Ag^+ ions and high stability [9–16].

The interest in silver materials, especially semiconductors, dates back to the early years of analog photography, but a resurgence has occurred with silver oxide-based ternary semiconductors such as silver vanadates [17,18]. The silver vanadate $AgVO_3$ has three polymorphic structures (α, β and γ), with the beta phase being the most stable under ambient temperature and pressure conditions [19]. It is also highly versatile [20–22], being applied as a photocatalyst [23–25], and a bactericidal material [24,26] as well as in batteries [27,28] and sensors [29]. In addition, $AgVO_3$ has antimicrobial activity against some pathogens such as *C. albicans*, *S. aureus*, *E. coli*, *P. aeruginosa*, *L. fermentum*, *B. subtilis*, *E. faecalis*, *C. horii*, *F. guttiforme* and *S. enterica* [30–34]. The silver vanadate $Ag_4V_2O_7$, on the other hand, is used as a photocatalyst for organic pollutants that are harmful to the environment [35–37]. These vanadates and other nanostructured semiconducting surfaces are useful as antimicrobial agents since they can generate ROS and reduce cell adhesion via neutralization of electrostatic forces, thus damaging the microbial cells [38].

The main challenge in obtaining a good antimicrobial material is to reach a balance between its activity and toxicity to humans, animals and plants. In many cases, excellent antimicrobial agents may also cause undesirable toxicity to animals and vegetables organisms. For instance, the release of Ag^+ and V^{4+}/V^{5+} from Ag/β-$AgVO_3$ incorporated into dental resin caused cytotoxicity in mouse fibroblast L929 cells [39]. Cytotoxic effects on human gingival cells (HGF) were also observed as a result of the release of Ag/β-$AgVO_3$ ions incorporated into commercial endodontic cements – even though genotoxic effects were not found [40]. In aquatic environments, Artal et al. reported that above 1 μg/L, Ag/β-$AgVO_3$ showed cytotoxic activity against the microcrustacean *Daphnia similis* [41]. At minimal inhibitory concentrations (MIC) to the fungus *C. albicans*, α-$AgVO_3$ did not have cytotoxic nor genotoxic effects against human keratinocytes (NOK-SI) [42]. All these results evidence that the toxicity analysis is crucial for the safe use of these materials.

In this work, we report the synthesis of the silver vanadates $AgVO_3$ and $Ag_4V_2O_7$ and their heterostructures by a simple precipitation process. The rationale behind the synthesis of such heterostructures involves the minimization of the detrimental electron (e^-)-hole (h^+) recombination that is typical of vanadates, as this recombination shortens the lifetime of charge carriers and limits their availability for producing ROS. Additionally, the e^--h^+ recombination can be suppressed in semiconductor-semiconductor heterostructures with appropriate band alignment [43], since $AgVO_3$ and $Ag_4V_2O_7$ are known to form heterostructures with metals and/or other semiconductors [26,33,44]. To the best of our knowledge, this is the first study exploring $Ag_4V_2O_7$/β-$AgVO_3$ heterostructures, which proved to have enhanced activity against *K. pneumoniae* in comparison with the pure vanadates. Lastly, the cytotoxicity and phytotoxicity of the vanadates were also analyzed.

2. Experimental section

2.1. Synthesis of $Ag_4V_2O_7$ powder

The $Ag_4V_2O_7$ powder was synthesized by chemical precipitation, as adapted from Oliveira et al. [20]. Initially, 2.10^{-3} mol of ammonium metavanadate (NH_4VO_3; 99.0 %, Sigma-Aldrich; CAS Reg. No. 7803-55-6) was dissolved in 50 mL of distilled water under magnetic stirring and then heated for complete solubilization. Afterwards, 4×10^{-3} mol of silver nitrate ($AgNO_3$; 99.8 %, Cennabras; CAS Reg. No. 7761-88-8) was solubilized in 50 mL of distilled water, followed by a few drops of ammonium hydroxide (NH_4OH) (30 % in NH_3, Synth) until the solution became clear. Both solutions were kept at 30 °C and mixed, causing the immediate release of the silver precursor onto the vanadate precursor and giving rise to the formation of the $Ag_4V_2O_7$ precipitate (yellowish precipitate). The mixture was centrifuged, and the precipitate was washed several times with distilled water and finally dried at 60 °C in an oven for 12 h.

Table 1
Proportion of each component and nomenclature of the heterostructures.

Nomenclature	$Ag_4V_2O_7$ (mol)	β-$AgVO_3$ (mol)
100:1	0.100	0.001
50:1	0.100	0.002
20:1	0.100	0.005
10:1	0.100	0.010

2.2. Synthesis of β-$AgVO_3$ powder

The synthesis of β-$AgVO_3$ powder was performed via chemical precipitation, according to a procedure adapted from a previous work [45]. At first, 1×10^{-3} mol of ammonium metavanadate (NH_4VO_3; 99.0 %, Sigma-Aldrich; CAS Reg. No. 7803-55-6) was dissolved in 50 mL of distilled water under magnetic stirring followed by heating for complete solubilization. Subsequently, a clear solution of 1×10^{-3} mol of silver nitrate ($AgNO_3$; 99.8 %, Cennabras; CAS Reg. No. 7761-88-8) was formed in 50 mL of distilled water. Both solutions were heated to approximately 60 °C and mixed, leading to the release of the silver precursor onto the vanadate precursor and forming the β-$AgVO_3$ precipitate (orange color). The mixture was then centrifuged, and the precipitate was washed several times with distilled water and dried at 60 °C in an oven for 12 h.

2.3. Synthesis of $Ag_4V_2O_7$/β-$AgVO_3$ heterostructures

The heterostructures were formed by ultrasonic mixture. The proportions listed in Table 1 were chosen because they yielded a uniform coating. Higher amounts of β-$AgVO_3$ than those shown in Table 1 caused non-surface leftovers in the $Ag_4V_2O_7$ particle, while lower amounts were insufficient for an effective coating. The quantities chosen, which were equivalent to x mol (x = 0.001, 0.002, 0.005 and 0.010) of β-$AgVO_3$ powder, were dispersed in 20 mL of distilled water using an ultrasonic bath for 20 min. The four 0.100 mol $Ag_4V_2O_7$ solutions in Table 1 were separately dispersed in 20 mL of distilled water using an ultrasonic bath for 20 min. The ultrasonic treatment was carried out to enhance the dispersion of powders. For decoration, each $Ag_4V_2O_7$ solution was added to the β-$AgVO_3$ solution under an ultrasonic bath, and the mixture was stirred for 20 min at room temperature. The powder samples were centrifuged, washed with distilled water, and dried in a conventional furnace at 60 °C for 24 h. The heterostructures were thereafter named 100:1, 50:1, 20:1 and 10:1, respectively.

2.4. Characterizations

The samples were characterized by X-ray diffraction (XRD) using a D/Max-2500PC diffractometer (Rigaku, Tokyo, Japan) and Cu Kα radiation (λ = 1.5406 Å) in the 2θ range of 15–65° and a scanning speed of 1° min^{-1}. The peaks were indexed according to standards of the Inorganic Crystal Structure Data (ICSD). Fourier-transform infrared spectroscopy (FTIR) was performed at room temperature using a Jasco FT/IR-6200 spectrophotometer (Japan) operating in absorbance mode. The spectra have a resolution of 4 cm^{-1} and 32 accumulations per measurement in the range of 400–4000 cm^{-1}. These measurements were performed on 12-mm diameter pellets containing 1 % by weight of each sample mixed with 99 % by weight of KBr (99 %, Sigma-Aldrich). Micro-Raman spectra were recorded using an iHR550 spectrometer (Horiba Jobin-Yvon, Kyoto, Japan) coupled to a silicon CCD detector and an argon-ion laser (Melles Griot, Rochester, NY USA) operating at 514.5 nm and with a maximum power of 200 mW. A fiber optical microscope was also employed. The morphological characteristics of the materials were examined using an Inspect F50 scanning electron microscope (SEM)

(FEI, The Netherlands) adjusted to an acceleration voltage of 5 or 20 kV and at a working distance of 3 mm. The samples were prepared by dispersing the powders in water and then depositing them on metal Si plates. Transmission electron microscopy (TEM) and high-resolution TEM (HR-TEM) were performed on a Jeol JEM 2100 Plus microscope operating at 200 kV. High-angle annular dark-field (HAADF) image and elemental mapping by energy-dispersive X-ray spectroscopy (EDS) were recorded in scanning TEM (STEM) mode. UV−Vis spectroscopic measurements were carried out with a Cary 5G spectrometer (Varian, USA) in diffuse reflection mode, in the wavelength range of 800 to 200 nm and at a scan speed of 600 nm/min. Photoluminescence (PL) measurements were performed at room temperature with the samples excited by a 355-nm laser (Cobolt/Zouk) focused on a 200-μm spot at a constant power of 5 mW. All deconvolutions were made using Voigt area function in PeakFit software (version 4.05).

2.5. Antimicrobial activity

For the antimicrobial activity, we choose four different strains of *Klebisella pneumoniae*: *K. pneumoniae* ATCC 1706, a standard strain; *K. pneumoniae* A54970, a multidrug-resistant carbapenemase (KPC)-producing strain; *K. pneumoniae* A34057, a multidrug-resistant strain capable of producing extended spectrum beta-lactamases (ESBL); and a community-isolated strain, *K. pneumoniae* A58240. KPC and ESBLs are enzymes that confer resistance to most carpabenem-like and beta-lactam antibiotics respectively, including third-generation cephalosporins and monobactams, and they are often seen in combination with other resistance mechanisms, causing multidrug resistance [46,47].

The antimicrobial activity of the samples was determined through the minimum inhibitory concentration (MIC) using the broth microdilution method with a 96-well plate, according to standard protocols (CLSI, 2008). The samples were dispersed in a Mueller Hinton Broth (Oxoid) with initial concentration of 2000 μg/mL, followed by the addition of each bacterial strain into their respective wells at 5×10^5 CFU/mL. Each plate was supplemented with vehicle (% DMSO), positive and negative controls. MIC was determined after incubation for 24 h at 37 °C through the lowest concentration of compound that inhibits bacterial growth. The results were performed in triplicate, on three different occasions. After the MIC determination, aliquots of 50 μL from all the wells which showed no visible bacterial growth were seeded on BHI agar plates and incubated for 24 h at 37C. When 99.9 % of the bacterial population is killed at the lowest concentration of an antimicrobial agent, it is termed as minimum bactericidal concentration (MBC) endpoint. This was done by observing pre- and post-incubated agar plates for the presence or absence of bacteria.

2.6. Cultivation of 3 T3 fibroblasts

Mouse 3 T3 fibroblasts were used. The cells were cultured in culture media bottles in DMEM High Glucose medium (Dulbecco's Modified Eagle Medium, Sigma-Aldrich, USA) in the presence of 100 μL/mL of penicillin/streptomycin antibiotics (LGC Biotechnology) with the addition of 10 % fetal bovine serum (FBS) inactivated by heat (LGC Biotechnology). The bottles were kept incubated in a humid environment at 37 °C and 5 % CO_2 until reaching 90 % confluence under passages.

2.7. Cell viability by MTT and neutral red assays

To evaluate the cell viability of mouse 3 T3 fibroblasts after 24 h of exposure to different concentrations of heterojunction 10:1, colorimetric assays were performed with the MTT salt and the neutral red dye. Since the MTT salt ((4,5 - dimethylthiazol - 2 - yl) 2,5 - diphenyl-bromide) (Sigma-Aldrich) is transformed into formazan crystals by mitochondrial enzymes of healthy cells, the greater the production of these crystals, the greater the cell viability [48]. As for the assay with the neutral red dye (Êxodo Científica®), it is based on the dye accumulation in liposomotropic membranes. Therefore, the more viable cells, the greater the diffusion of the dye through the membrane [49]. We used a flat-bottom 96-well microplate to inoculate 1×10^4 cells per well. After 24 h of adherence material with different concentrations were added, and after 24 h of exposure the wells were washed with 1× PBS (phosphate buffer saline: 8 g of NaCl, 0.2 g of KCl, 1.15 g of Na_2HPO_4, 0.2 g of KH_2PO_4 and 1 L of distilled water), and 200 μL of MTT solution (0.5 mg/mL in 1× PBS plus incomplete DMEM medium without phenol [1:5]) and 100 μL of neutral red dye (30 μg/mL in DMEM medium supplemented with 1 % FBS (fetal bovine serum) and without phenol) were added. The reaction took place for 3 h for the MTT assay and for 2 h for the neutral red assay, both at 37 °C and 5 % CO_2. Blank controls containing only MTT and NR (neutral red) solution were also prepared. Afterwards, the reagent solution was removed and 100 μL of DMSO diluent was added per well for the MTT assay, while 200 μL of diluent containing 50 % ethanol and 1 % acetic acid (1:1) was added per well for the assay with NR. Then, absorbance measurements were carried out at 570 nm (MTT) and 540 nm (NR) using a spectrophotometer (Thermo Scientific™ Multiskan™ GO Microplate). Cell death control (CTRL+) was performed with 5 % extran enzymatic detergent (MTT). The percentage of cytotoxicity was calculated by comparing the data with the CTRL- group according to Eq. (1) below:

$$\%cytotoxicity = \frac{experimental\ group}{mean\ of\ the\ control\ group} x100 \quad (1)$$

2.8. Cell morphology by optical microscopy

For the analysis of cell morphology of mouse 3 T3 fibroblasts we used a flat-bottom 96-well microplate to inoculate 1×10^4 cells per well. After 24 h of adherence material with different concentrations were added, and after an exposure of 24 h the wells were observed using an Axiovert 40 CFL optical microscope (Zeiss) with a 10× objective lens. The images were captured with a coupled camera model LOD-3000 (Bio Focus) and analyzed using Future WinJoeTM software version 2.0 at a 100× final resolution.

2.9. Production of reactive nitrogen species (RNS) through Griess reaction

To measure the production of RNS through Griess reaction, the production of nitrite ion (NO_2) was also monitored [50,51]. On a flat-bottom 96-well microplate, 1×10^4 cells per well were inoculated, with treatments being added after 24 h of adherence. The wells were then washed two times with 1× PBS after a 24 h exposure, and 50 μL of supernatant was collected and added to a new plate followed by the addition of 50 μL of Griess solution (1:1 mixture of solution A [1 % sulfanilamide in 5 % phosphoric acid] and solution B [0.1 % N-1-naphthylethylenediamine dihydrochloride]) for 15 min at room temperature. The absorbance at 554 nm was measured using a spectrophotometer (Thermo Scientific™ Multiskan™ GO Microplate). The concentration of nitrite in the supernatant was quantified from a standard curve with known concentrations of nitrite (expressed in mM) described in the kit.

2.10. Detection of reactive oxygen species (ROS) by fluorescent probe DCFH-DA

ROS production was measured using the fluorescent probe DCFH-DA (2′,7′-Dichlorodihydrofluorescein Diacetate) (Sigma-Aldrich). 1×10^4 cells per well were inoculated into a black flat-bottomed, clear-bottomed 96-well microplate. After 24 h of adhesion, materials with different concentrations were added. After the 24-h exposure times, the wells were washed 2 times with 1× PBS and 100 μL of the 100 mM probe diluted in DMEM without FBS were added. The reaction took place for 30 min at 37 °C and 5 % CO_2 protected from light. The reagent solution

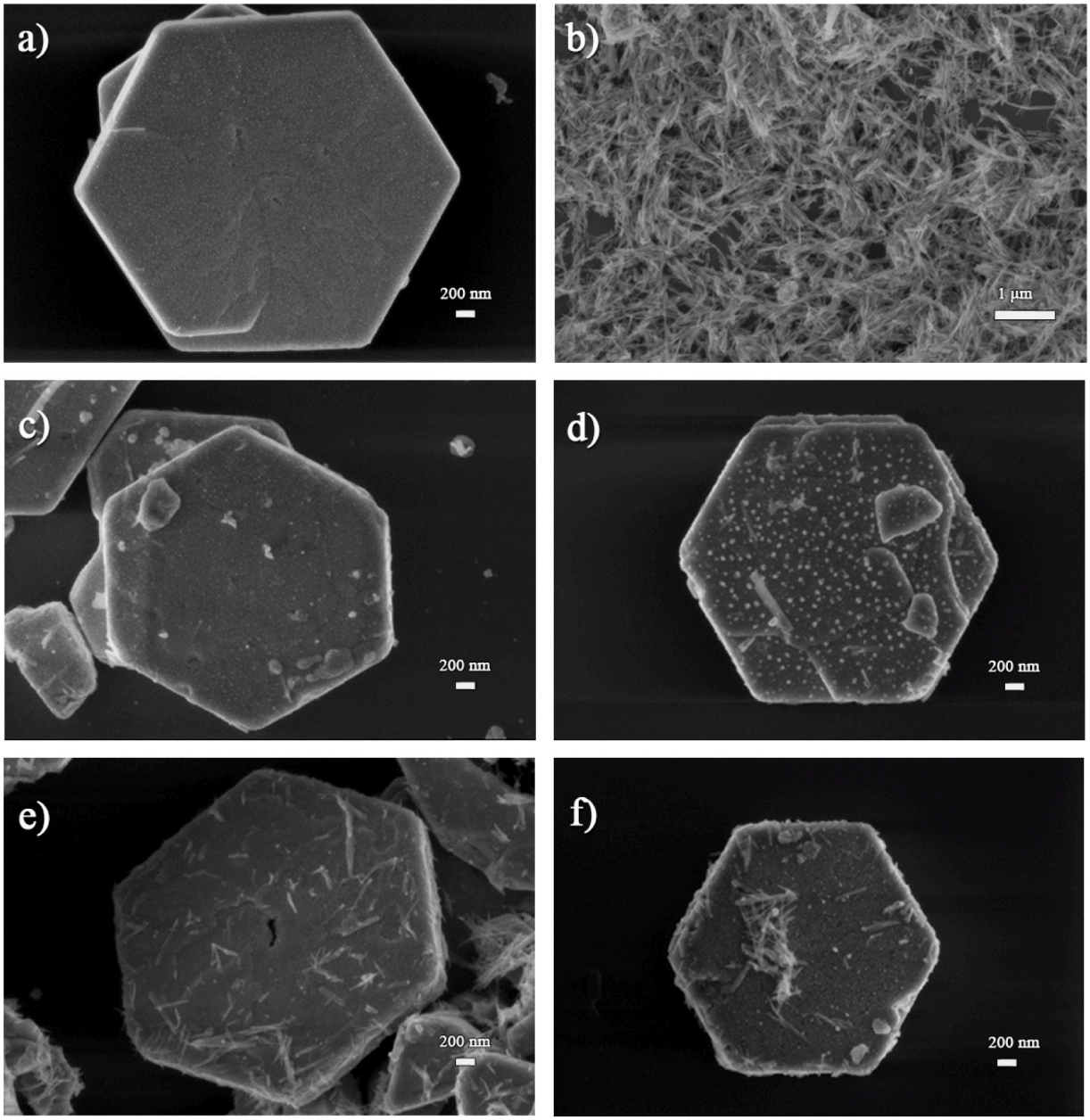

Fig. 1. Morphological characterization by SEM of a) $Ag_4V_2O_7$, b) β-$AgVO_3$ and heterostructures: c) 100:1 d) 50:1, e) 20:1 and f) 10:1.

was then removed and the wells washed with PBS 1× followed by the addition of an additional 100 µL of PBS per well, followed by reading the absorbance at 485–530 nm on the Spectra MAX i3® plate spectrophotometer (Molecular Devices). The values obtained will be transformed into percentages using Eq. (1).

2.11. Identification of ROS produced by the material

To probe the role of ROS along the biocidal process, scavenger measurements were performed. A total of 50.0 mg of each sample was added in equivalent amounts: ammonium oxalate (AO, $(NH_4)_2C_2O_4.H_2O$; 99.5 %, Aldrich), *p*-benzoquinone (BQ, $C_6H_4O_2$, Merck), silver nitrate (SN, $AgNO_3$; 99.8 %, Vetec) and ascorbic acid (AA, $HC_6H_7O_6$; 99.5 %, Aldrich), acting as scavengers for h^+, superoxide radicals ($^{\bullet}O_2^-$), e^- and hydroxyl radicals ($^{\bullet}OH$), respectively. These equivalent amounts were added to 50.0 mL of Rhodamine B (RhB, $C_{28}H_{31}ClN_2O_3$; 99.8 %, Synth) solution (1×10^{-5} mol L^{-1}). The solution was placed in an ultrasound bath for further particle dispersion and left in the dark for 30 min at 25 °C under constant stirring. Then, the 6-lamp UV–Vis light (PHILIPS TL-D, 15 W, 3.6 mV/cm^2) was switched on and an aliquot was removed after an irradiation of 120 min. The aliquot was analyzed on an absorption spectrophotometer in the UV–Vis region (V-660 spectrophotometer, JASCO) by monitoring the decrease in the characteristic RhB peak at 554 nm.

2.12. Phytotoxicity

The effect of $Ag_4V_2O_7$, β-$AgVO_3$ and $Ag_4V_2O_7$/β-$AgVO_3$ heterostructures (10:1) on the growth of *Lactuca sativa (L. sativa)* and *Cucumis sativus (C. sativus)* plants was evaluated according to the method described by Dória et al. [52] and Wang et al. [53]. Briefly, the seeds were disinfected for 15 min with 4 % sodium hypochlorite and then washed with distilled water. Subsequently, 20 seeds of each cultivar were separated on a Petri dish with filter paper (80 mg/cm^2), put into contact with 4 mL of sample solutions (at concentrations of 10,000 µg/mL, 1000 µg/mL, 100 µg/mL, 10 µg/mL and 1 µg/mL), closed with PVC

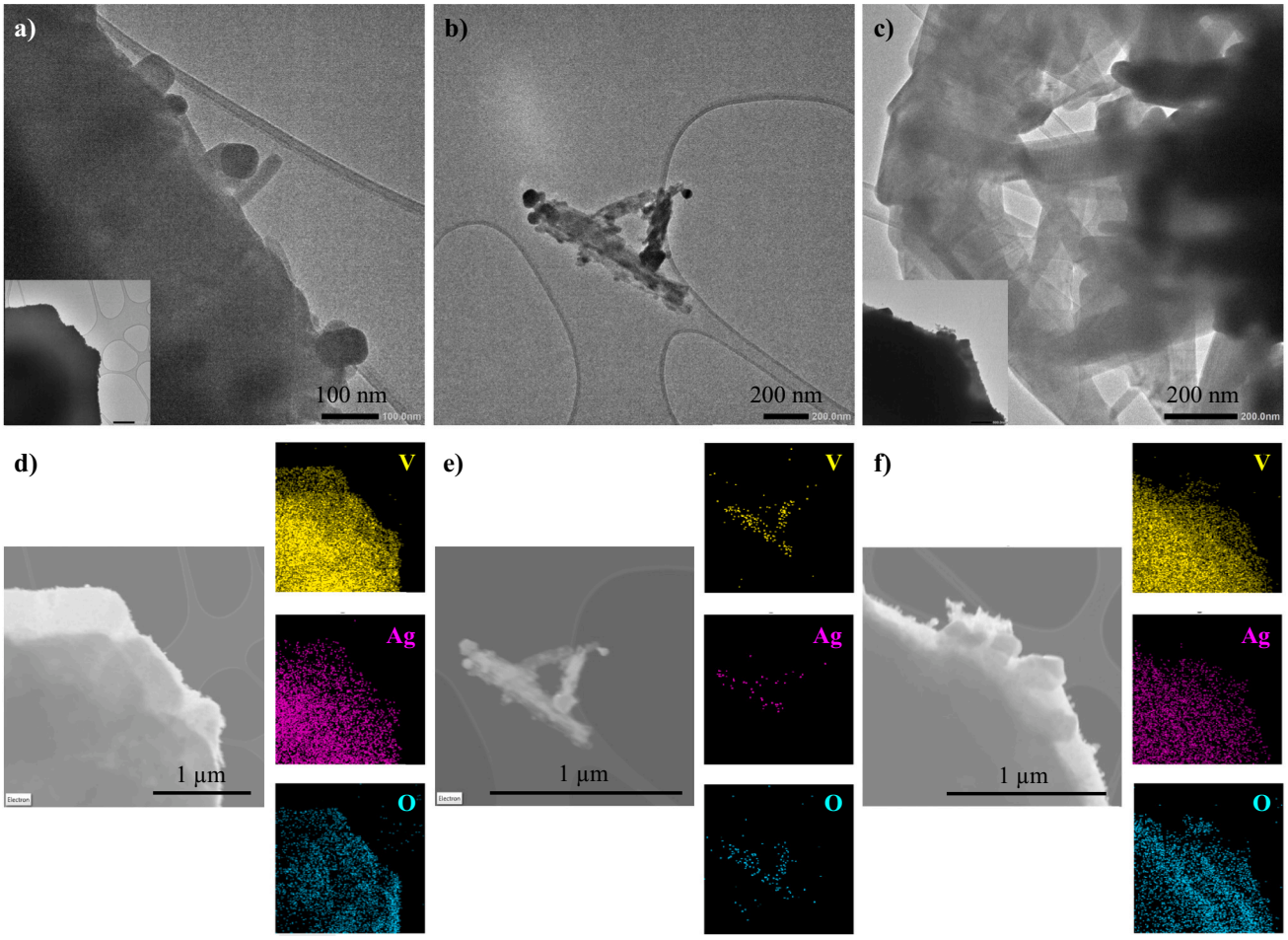

Fig. 2. Low-magnification TEM images of (a) $Ag_4V_2O_7$, (b) β-$AgVO_3$ and (c) heterostructure 10:1, and EDS mappings of (d) $Ag_4V_2O_7$, (e) β-$AgVO_3$ and (f) heterostructure 10:1.

film paper in order not to lose moisture, and kept at 22 ± 3 °C for 5 days without any exposure to light. As a negative control, 4 mL of distilled water was used. The results were performed in triplicate. After 5 days, the number of germinated seeds and root lengths was used to calculate the germination indices (GI) and relative growth indices (RGI) through Eqs. (2) and (3):

$$GI = \frac{RLS\ x\ NGS}{RLC\ x\ NGC} \times 100 \quad (2)$$

$$RGI = \frac{RLS}{RLC} \times 100 \quad (3)$$

where RLS is the relative length of the sample root, RLC is the relative length of the control root, NGS is the number of germinated seeds in the sample, and NGC is the number of germinated seeds in the control.

2.13. Statistical analysis

The data in this study are expressed as mean ± SD and analyzed using GraphPad Prism 7.0 (San Diego, California, USA) and Sigmaplot software (version 14). The entire study was performed in biological triplicates, at least, and in three independent experiments. The data were analyzed using Shapiro-Wilk test, analysis of variance by Brown-Forsythe test, analysis with One-Way RM ANOVA to verify the parametric or non-parametric nature of the data and post-hoc test of Tukey's multiple comparisons. Results are presented as the median with upper and lower quartiles: Me [Q1; Q3]. Statistical significance was set at $p < 0.05$.

3. Results and discussion

The structural analysis of $Ag_4V_2O_7$, β-$AgVO_3$ and $Ag_4V_2O_7$/β-$AgVO_3$ heterostructures (10:1, 20:1, 50:1 and 100:1) by XRD, Raman, FTIR and PL revealed the formation of the pure $Ag_4V_2O_7$ and β-$AgVO_3$ and the heterostructures, as shown in detail in the *Supporting Information* (Figs. S1–S7 and Tables S1–2). Microhexagons with average size of ca. 2.7 µm in width and 1 µm in thickness corresponding to $Ag_4V_2O_7$ can be seen in the SEM image in Fig. 1a, while nanorods with diameters of 45–70 nm corresponding to β-$AgVO_3$ can be observed in Fig. 1b. These images are consistent with the literature [20,52]. Fig. 1c–f reveal β-$AgVO_3$ nanorods on the surface of $Ag_4V_2O_7$ microhexagons, confirming the formation of $Ag_4V_2O_7$:β-$AgVO_3$ heterostructures. In addition, such microhexagons are not completely covered by the nanorods, thus causing the surfaces of both vanadates to be available for interaction with the microorganisms in the surrounding medium. Moreover, there may be electron transfer between both semiconductors, which is relevant to ROS production, as discussed later on.

The TEM images in Fig. 2 show the $Ag_4V_2O_7$ microhexagons, the β-$AgVO_3$ nanorods and the interface between $Ag_4V_2O_7$ and β-$AgVO_3$ particles where it is possible to observe that the $Ag_4V_2O_7$ microhexagon is covered by β-$AgVO_3$ nanorods. Irregular spherical nanocrystals in Fig. 2a–b are due to an instability of the silver vanadate structure exposed to electron beam irradiation, which ends up creating Ag^0 nanocrystals. The elemental composition was investigated using EDS mappings (Fig. 2d–f), with the colors assigned to the elements V (vanadium, yellow color), Ag (silver, yellow color) and O (oxygen, cyan color). These elements have overlapped profiles and coincide with the

Table 2
Minimal inhibitory and bactericidal concentrations (MIC/MBC) for $Ag_4V_2O_7$, β-$AgVO_3$ and heterostructures in *K. pneumoniae* strains.

	K. pneumoniae	$Ag_4V_2O_7$	100:1	50:1	20:1	10:1	β-$AgVO_3$
MIC/MBC (μg/mL)	ATCC 1706	125	125	125	31.25	31.25	125
	A54970	125	62.5	62.5	62.5	62.5	125
	A34057	125	62.5	62.5	62.5	31.25	125
	A58240	125	125	62.5	62.5	31.25	125

Table 3
MIC values for the activity of silver vanadates against different microorganisms and other silver-based materials against *K. pneumoniae*.

Microorganisms	Material	MIC (μg/mL)	Reference
K. pneumoniae (ATCC 1706)	$Ag_4V_2O_7$:β-	31.25	This work
K. pneumoniae (A54970)	$AgVO_3$	62.5	
K. pneumoniae (ATCC 51503)	Ag^0	33.75	[77]
K. pneumoniae (K5)		67.5	
K. pneumoniae (K112)		33.75	
K. pneumoniae	Ag^0	300	[78]
S. aureus (MRSA ATCC 33591)	α-$AgVO_3$	62.5	[15]
E. faecalis (ATCC 29212)	β-$AgVO_3$:Ag^0	500	[76]
P. aeruginosa (ATCC 27853)		31.25	
E. coli (ATCC 25922)		31.25	
S. aureus (ATCC 25923)	β-$AgVO_3$:Ag^0	31.25	[77]
S. mutans (ATCC 25175)		250	
P. aeruginosa (ATCC 27853)		31.25	
C. albicans (ATCC 10231)		62.5	
S. aureus (MRSA ATCC 33591)	α-$AgVO_3$:HA 1	1000	[33]
&	α-$AgVO_3$:HA 6	250	
S. aureus (MSSA ATCC 25923)	α-$AgVO_3$	125	
E. coli	β-$AgVO_3$	100	[79]
L. innocua		150	
S. aureus		50	

main microhexagons and nanorods in Fig. 2a–c, evidencing the β-$AgVO_3$ and $Ag_4V_2O_7$ structures.

The processes involved in the inactivation of *K. pneumoniae* by these materials as antimicrobial agents can occur via electrochemical [54], photochemical and photocatalytic processes [55]; however, it may also take place in dark environments when mediated by semiconductors [56,57]. Herein, we tested $Ag_4V_2O_7$, β-$AgVO_3$ and the heterostructures (10:1, 20:1, 50:1 and 100:1) against four strains of *K. pneumoniae*, one with standard characteristics (ATCC 1706); two of them (A34057 and A54970) classified as resistant; and one community-isolated (A58240). According to Table 2, total inhibition of all *K. pneumoniae* strains was reached with only 125 μg/mL of $Ag_4V_2O_7$ or β-$AgVO_3$. An even higher efficiency was obtained with the heterostructures due to their synergistic effects. The inhibition of *K. pneumoniae* A54970 and A34057 was achieved with the heterostructures 20:1, 50:1 and 100:1 at 62.5 μg/mL. For *K. pneumoniae* ATCC 1706, *K. pneumoniae* A34057 and *K. pneumoniae* A58240, a concentration of 31.25 μg/mL of the heterostructures 10:1 was found to be effective for inhibition. The MIC values for the heterostructures against *K. pneumoniae* in Table 3 are lower than those reported in the literature for silver- and silver vanadate-based materials. The suspension from the wells with no turbidity of each strain was inoculated in BHI agar plate and incubated for 24 h. No bacteria growth was observed in any of the concentrations, hence confirming the bactericidal activity and indicating that the MIC is equal to the MBC.

The cytotoxicity of heterostructure 10:1 was analyzed using 3 T3 murine cells, which are normal and healthy mouse embryonic fibroblasts from Swiss embryos [58]. This cell line is often used for preliminary screening of materials prior to in vivo evaluation. This heterostructure was chosen because it presents one of the best MIC results and has the highest amount of β-$AgVO_3$. Five concentrations of this heterostructure were chosen: two above and two below the MIC value. MTT salt and NR dye assays were employed, as these are typical assays for drug screening [59]. The heterostructure decreased the percentage of cell viability in 3 T3 fibroblasts after 24 h exposure in all concentrations and in both MTT and NR assays, as demonstrated in Fig. 3A–B. This cytotoxicity was found in dental applications based on β-$AgVO_3$ tested in human gingival fibroblasts (FGH strain) [60]. The cell viability of FGH, THP-1 (leukemic monocytes) and NOK-SI (oral keratinocytes) was also observed using α-$AgVO_3$, α-Ag_2WO_4, and β-Ag_2MoO_4 microcrystals [34]. A qualitative analysis of cell morphology was made 24 h after exposure to different concentrations of heterostructure 10:1. The images in Fig. 3C indicate changes in cell morphology induced by the heterostructure, with a lower number of viable cells, a decrease in cell size and a change in shape in comparison with the control group. These changes were observed for the concentrations of 31.25, 62.5 and 125 μg/mL, while cell morphology was preserved in the control group, which is consistent with the cell viability results. Cellular cytotoxicity may be related to several factors and be mediated by some pathways, such as the production of reactive nitrogen species (RNS) [59]. Fig. 3D shows that the number of RNS in 3 T3 cells exposed to the heterostructure at concentrations of 31.25, 62.5 and 125 μg/mL considerably increased in comparison with the control group. It is reported that the production of RNS induces cellular damage, resulting in nitrous stress [61]. In addition, it also impairs mitochondrial activity and may alter the cellular metabolic profile [62,63]. Fig. 3E shows the values in % of ROS generation compared to the control. There was intracellular production, but in a smaller amount than the control. Organisms exposed to oxygen produce ROS in their normal metabolism. In certain pathological situations, the production of these species increases. In both situations, the so-called oxidative stress occurs: reactive oxygen species are normally (but not always) powerful oxidizing agents that damage all types of cellular structure, from membrane lipids to DNA, as well as the RNS [64]. It is believed that ROS inhibition occurred due to the arrest in the cell cycle causing the cells to stay in G1, with no cell growth for phase S which corroborates the decrease in cellular viability [65]. This effect is connected with the contact of cells with the material, which can cause several adverse effects to these cells (such as extracellular ROS production, ionic release, stress by physical contact, etc). To avoid such cytotoxic effects with the $Ag_4V_2O_7$/β-$AgVO_3$ heterostructures in their free form, they need to be incorporated into coatings and polymers.

Once tested in animal cells, the toxic effect was analyzed in plant organisms, in order to understand the impacts of these materials on the development of L. *sativa* and *C. sativus*. The phytotoxicity of $Ag_4V_2O_7$, β-$AgVO_3$ and $Ag_4V_2O_7$:β-$AgVO_3$ (10:1) was analyzed through germination (GI) and relative growth indices (RGI) of the roots of L. *sativa* and *C. sativus* cultivars. Fig. 4 shows low GI and RGI rates compared to the control group for both cultivars at high sample concentrations. It can be noted that both the GI and RGI increased with decreasing concentrations, whereas no phytotoxic effect was observed at 1 μg/mL. It is known that β-$AgVO_3$ has lower phytotoxicity than the other samples and that L. *sativa* is more affected by $Ag_4V_2O_7$ than *C. sativus*. This phytotoxicity is related to the production of ROS by the vanadates. Seed exposure to ROS leads to high local oxidative stress, which in turn can cause starch degradation and seed calcification [66]. Moreover, these species are also identified as non-enzymatic growth factors of radicle elongation and endosperm weakening, which are essential for endosperm seed germination [67]. According to Leep et al., the contact of seeds with vanadium species can reduce seed growth and produce significant morphological changes [68]. Depending on the concentration, silver species can also impair plant growth and germination due to their interaction with

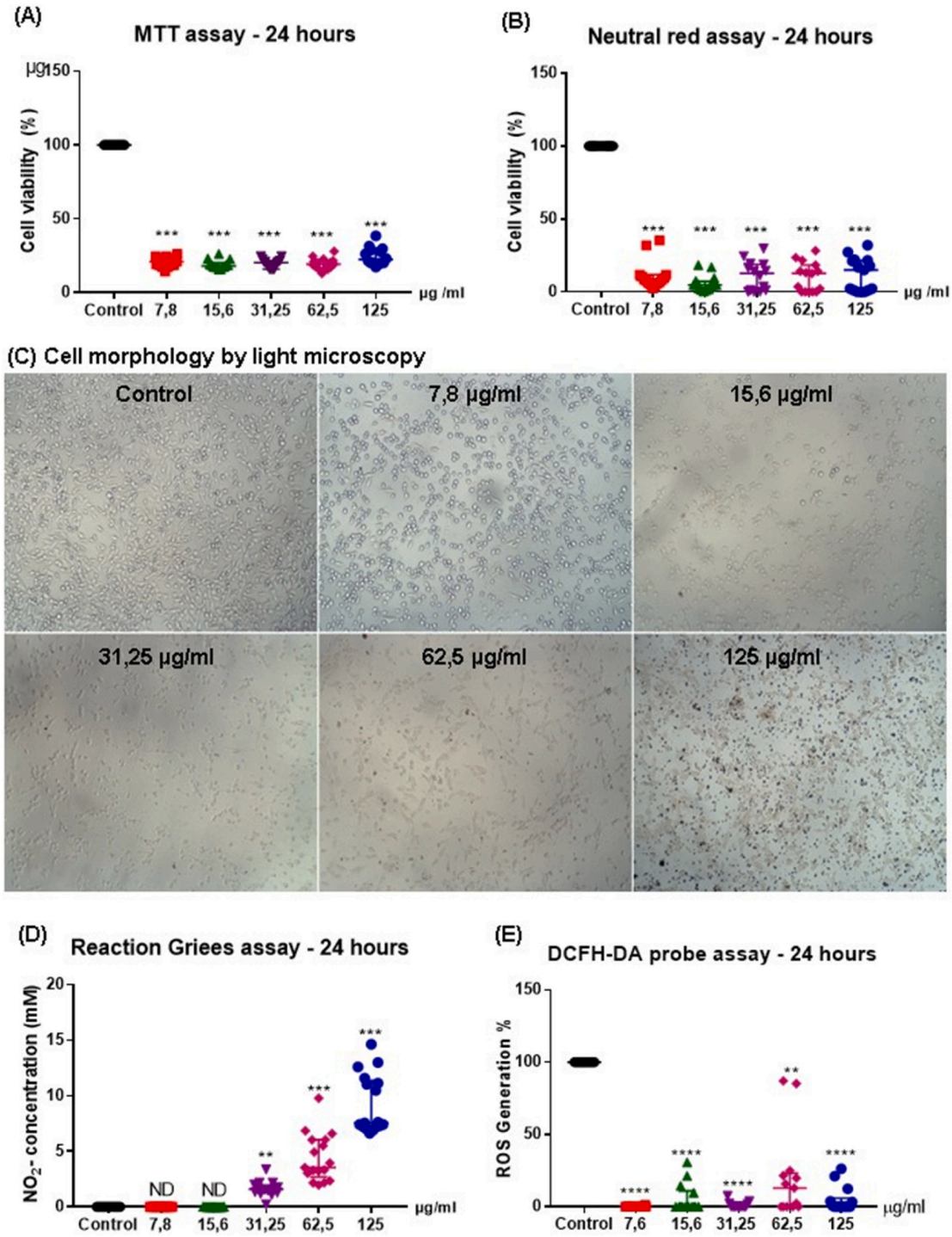

Fig. 3. Effect of heterostructure 10:1 on 3 T3 fibroblasts after 24 h exposure to different concentrations (125, 62.5, 31.25, 15.6 and 7.8 µg/mL) in comparison with control (cells + medium). (a) Cell viability (%) MTT and (b) Cell viability (%) NR. (c) Cell morphology of fibroblast. (d) NO production [concentration] vs. control. (e) ROS generation (%). *p < 0.5; **p < 0.01; ***p < 0.001; ****p < 0.005. The results were presented as the median with the upper and lower quartiles: Me [Q1; Q3].

functional groups in plant cells [69].

The mechanisms involved in the bactericidal, cytotoxic and phytotoxic activities are associated with the generation of reactive oxygen species (ROS), as demonstrated below. The ROS generation by $Ag_4V_2O_7$, β-$AgVO_3$ and their heterojunction (10:1) was quantified through RhB photodegradation tests. According to Table 4, there was an increased RhB photodegradation by the heterostructure, which was more effective for redox reactions and yielded more ROS than the pure silver vanadates. The species generated during photocatalysis was determined through scavenger tests using AA, SN, BQ and AO as scavengers for $^{\bullet}OH$, e^-, $^{\bullet}O_2^-$ and h^+, respectively. A significant decrease in the photocatalytic efficiency was observed for the scavengers BQ and AA, confirming that $^{\bullet}OH$ and $^{\bullet}O_2^-$ are the main species involved in the RhB photodegradation. Thus, it can be inferred that these species are also responsible for the bactericidal, cytotoxic and phytotoxic activities observed herein, being in congruence with the literature [10,33].

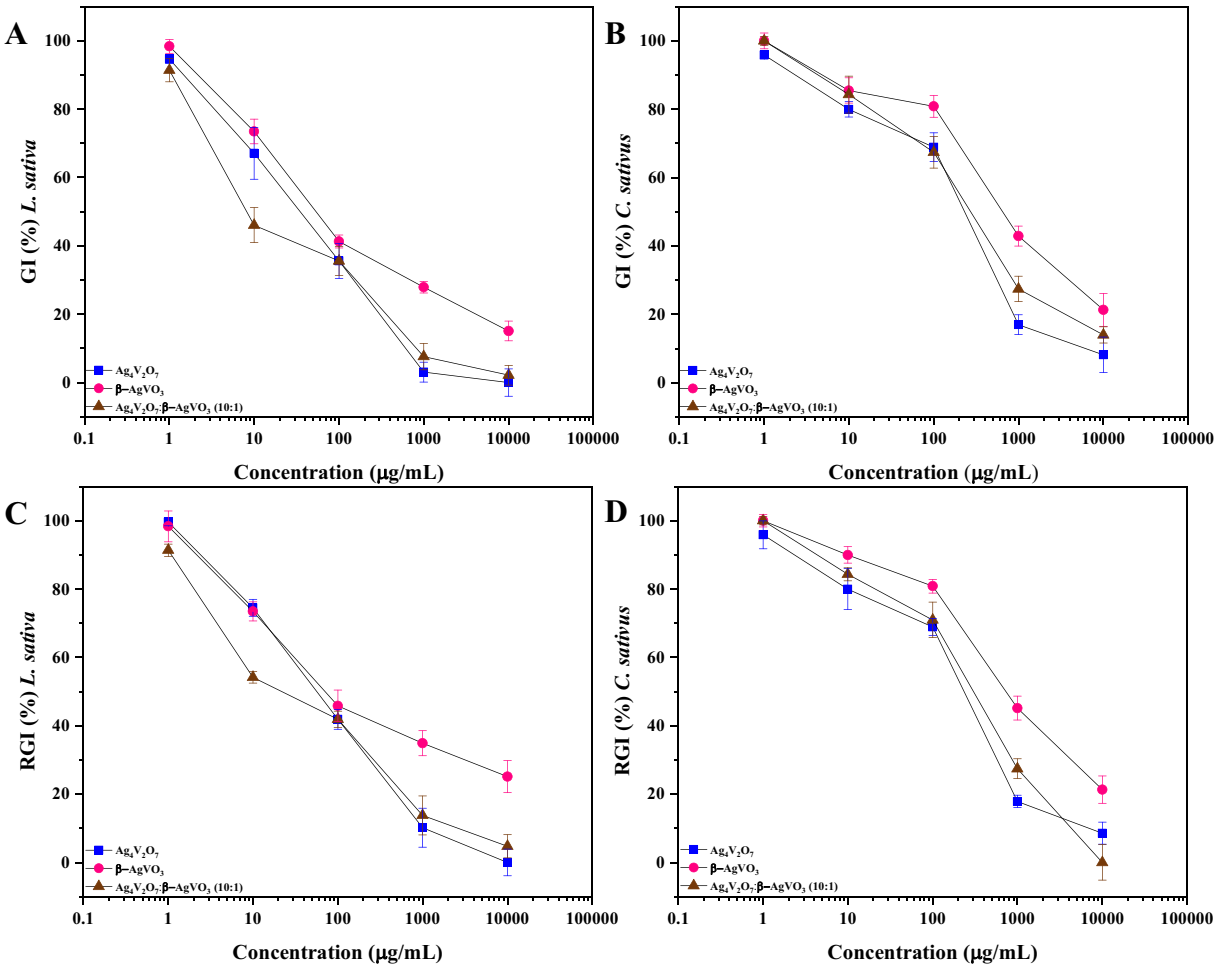

Fig. 4. GI (a, b) and RGI (c, d) rates for L. *sativa* and *C. sativus* cultivars against $Ag_4V_2O_7$, β-$AgVO_3$ and $Ag_4V_2O_7$:β-$AgVO_3$ (10:1).

Table 4
Identification of ROS generated by the semiconductor.

Scavengers	β-$AgVO_3$ (Efficiency; %)	$Ag_4V_2O_7$ (Efficiency; %)	$Ag_4V_2O_7$:β-$AgVO_3$ (Efficiency; %)
No scavenger	59	72	87
AO	59	71	70
AA	1	1	3
SN	45	72	75
BQ	6	11	9

The formation of heterojunctions in the heterostructures can be explained by analyzing the energy spectra of semiconductors. Their optical band gap, E_g, was estimated by extrapolating the linear portion of the UV−Vis spectra using the Kubelka−Munk function [70] and assuming n = ½, since both $Ag_4V_2O_7$ and β-$AgVO_3$ exhibited indirect transitions [19,71]. Results for $[F(R_\infty)h\nu]^2$ vs. $h\nu$ were plotted to determine the E_g values of the powders (Fig. 5). It can be seen that both $Ag_4V_2O_7$ and β-$AgVO_3$ had strong visible light absorption, with band gaps of 2.31 and 2.07 eV, respectively – which is consistent with the results reported in the literature [72].

Charge transfer processes between clusters from distinct structures are expected to take place in the heterostructure. Therefore, to obtain further information on its electronic structure, the energies associated with the edges of E_{CB} and E_{VB} for $Ag_4V_2O_7$ and β-$AgVO_3$ were estimated using Mulliken's theory of electronegativity:

$$E_{VB} = X + 0.5E_g - E^e \quad (4)$$

$$E_{CB} = E_{VB} - E_g \quad (5)$$

$$X = \left[\chi\,(A)^a \chi\,(B)^b \chi\,(C)^c\right]^{1/(a+b+c)} \quad (6)$$

$$\chi = \frac{1}{2}\,(E_{ea} + E_i) \quad (7)$$

where E_{VB} is the valence band edge potential, E_{CB} is the conduction band edge potential, E_g is the band gap energy, X is electronegativity or Sanderson electronegativity (a, b, c are the atom number of compounds), E^e is the energy of free electrons vs. hydrogen (4.5 eV), and χ is the Mulliken electronegativity, which is the arithmetic mean of the first ionization energy (E_i) of the metal and the electron affinity (E_{ea}) of each semiconductor atom [73]. Fig. 6 displays the band diagrams, where it is possible to observe that the E_g for $Ag_4V_2O_7$ and β-$AgVO_3$ is 2.31 eV and 2.07 eV, respectively. By using X and E_g, the E_{CB} and E_{VB} for $Ag_4V_2O_7$ are 0.07 eV and 2.38 eV, respectively, while the E_{CB} and E_{VB} for β-$AgVO_3$ are 0.33 and 2.40 eV, respectively (see Table S3). There are three different types of semiconductor heterojunctions, which are classified according to the positions of the valence (VB) and conduction bands (CB). The heterojunction between $Ag_4V_2O_7$ and β-$AgVO_3$ is type II (staggered gap), that is, the migration of charges can occur in opposite directions. In this configuration, e^- are accumulated in one semiconductor ($Ag_4V_2O_7$), while h^+ are accumulated in the other (β-$AgVO_3$) [74]. This behavior arises from the reorganization of defective energy states induced by changes in the structural order [75]. The importance of the electronic structure and charge distribution is confirmed by PL measurements

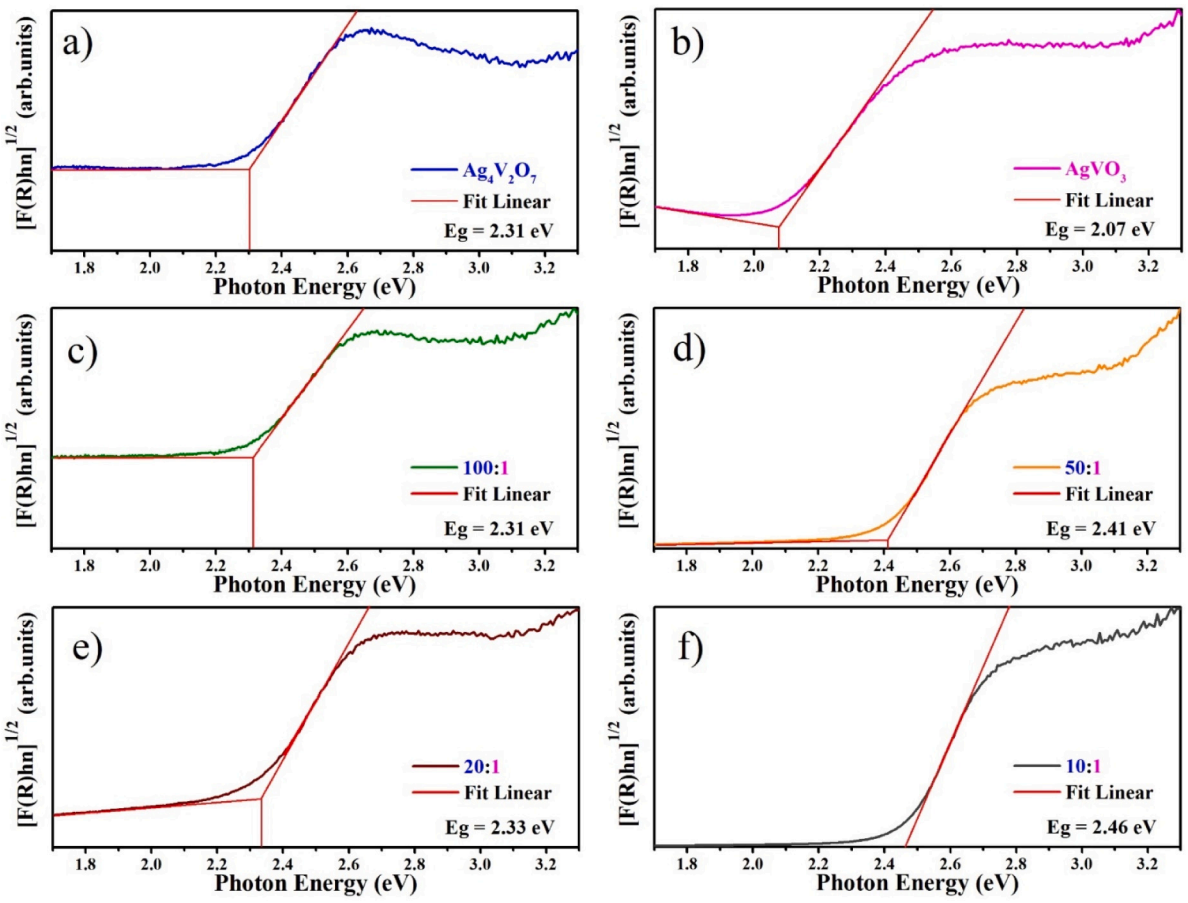

Fig. 5. UV–Vis spectra of (a) $Ag_4V_2O_7$, b) β-$AgVO_3$ and heterostructures: c) 100:1 d) 50:1, e) 20:1 and f) 10:1.

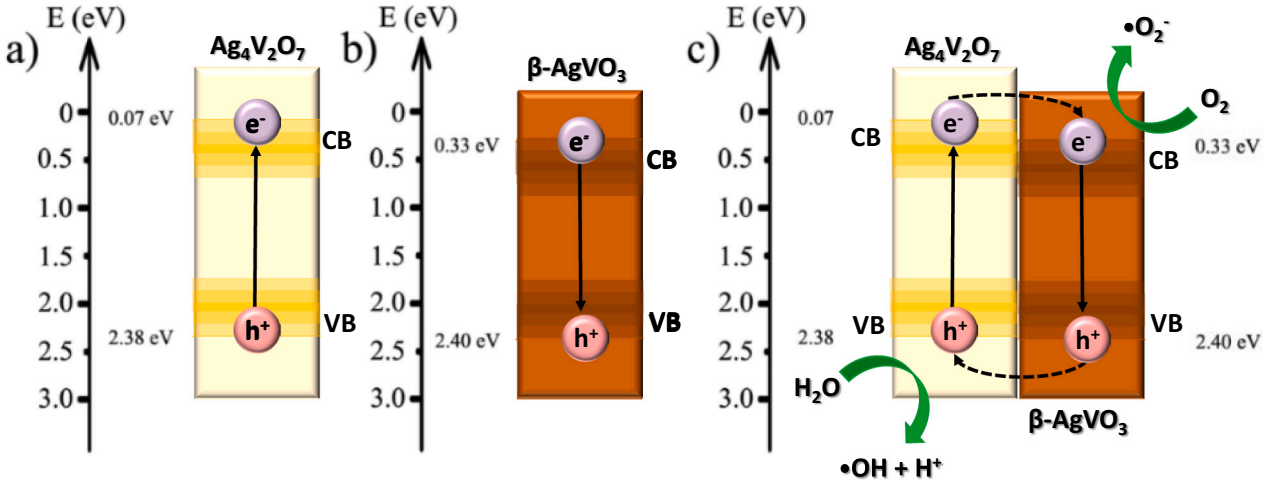

Fig. 6. CB and VB in a) $Ag_4V_2O_7$, b) β-$AgVO_3$, and C) $Ag_4V_2O_7$/β-$AgVO_3$ heterostructure.

(Figs. S4–S8). The flow of e^--h^+ pairs can be facilitated through the heterojunction, which increases the probability of redox reactions with the constituents of the used medium (i.e., H_2O, O_2 and organic molecules).

When ROS is produced by semiconductors, H_2O loses an e^- to form an •OH and a proton (H•). Simultaneously, an e^- is transferred to the O_2 molecule, forming a superoxide anion ($•O_2^-$). In turn, to maintain the balance of charge and mass this ion interacts with H•, forming a hydrogen peroxide radical (•OOH). ROS can then enters the microorganism membranes and reacts with the existing phosphate and sulfate groups, leading to cell death or preventing its replication by stopping the production of essential proteins [8] In limited amounts, ROS is required for cellular homeostasis and redox signaling. Sustained attack of endogenous and exogenous ROS results in conformational and oxidative changes in key biomolecules, lipid peroxidation, protein carbonylation, formation of carbonyl adducts (aldehyde/ketone), nitration, sulfoxidation, DNA damage, and oxidation of nucleobases [76]. Due to its short life-time, most of the damage caused by ROS occurs

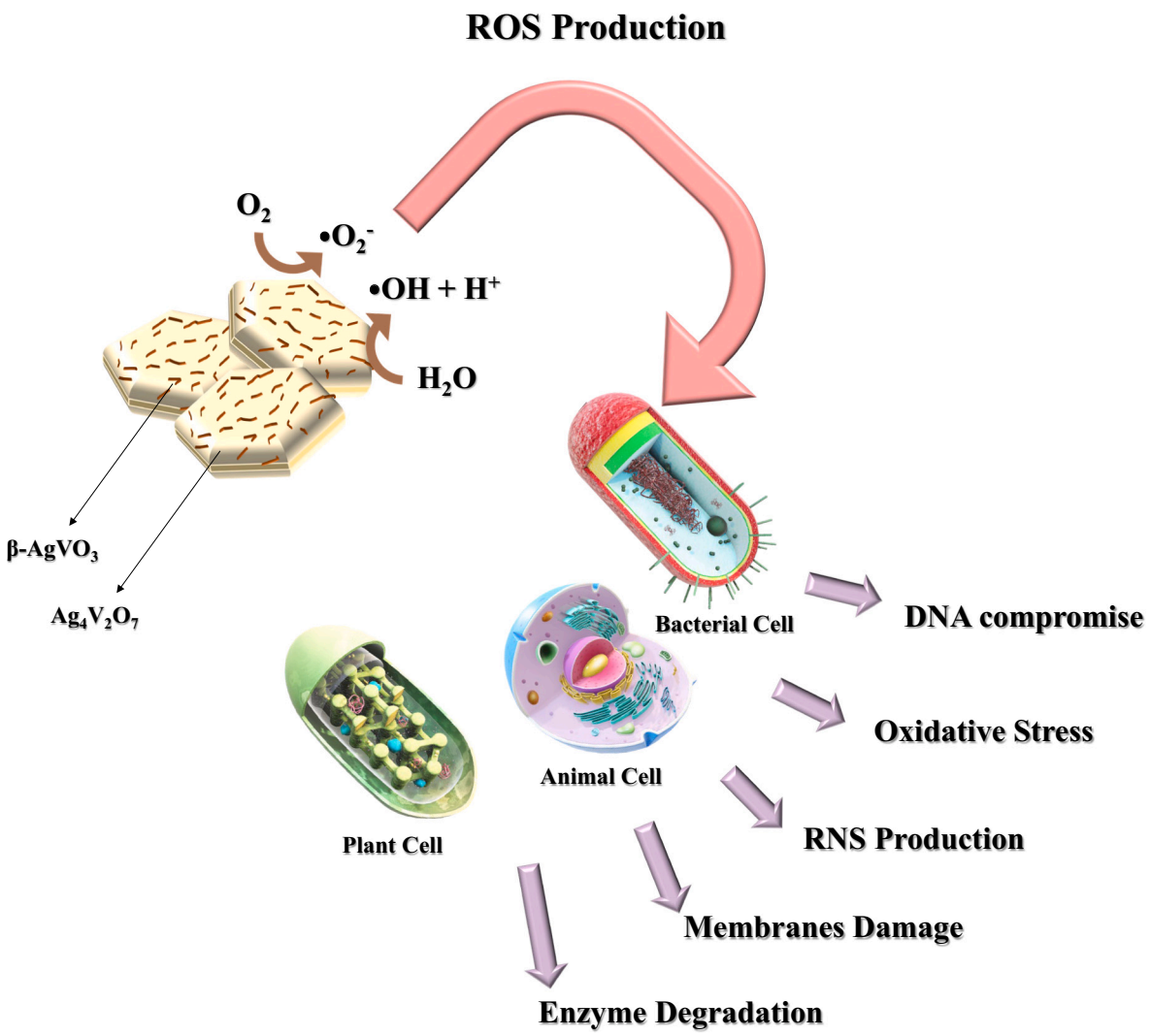

Fig. 7. Representative scheme of action of $Ag_4V_2O_7$/β-$AgVO_3$ heterostructures and their toxicity.

in the cell wall, interrupting the components of the respiratory chain and the cellular electrochemical potential, disabling the cell to generate energy, and leading to death. The fate of cells, most notably their survival or death, is determined by cellular responses to physiological conditions. Cells are regulated to maintain normal development and tissue homeostasis, in addition to offering protection against a variety of diseases. A representative scheme of these results is illustrated in Fig. 7.

4. Conclusions

We described the synthesis and characterization of $Ag_4V_2O_7$/β-$AgVO_3$ heterostructures, which proved to have the ability to kill *Klebsiella pneumoniae* ATCC 1706 and its antibiotic-resistant A54970 strain. The heterostructures were found to be more efficient than the free vanadates due to their increased ROS generation with consequent formation of hydroxyl (•OH) and superoxide ($\bullet O_2^-$) radicals. Unfortunately, the most efficient bactericidal agent, i.e., $Ag_4V_2O_7$/β-$AgVO_3$ heterostructure 10:1, was also considered to be toxic to mouse 3 T3 fibroblasts, besides exhibiting phytotoxicity above 1 μg/mL for the germination of *C. sativus* and L. *sativa* seeds. Therefore, practical applications of the proposed heterostructures are envisaged in coatings where leaching is avoided or encapsulated.

CRediT authorship contribution statement

M.A and **J.S·S**: Investigation, Project administration, Methodology, Validation, Data Curation, Visualization, Writing - Original Draft, Writing - Review & Editing. **M.O.G., J.M.A.R., B.D.L.F.**: Methodology, Validation, Formal analysis, Writing - Original Draft. **A.B.P.C.** and **L.K.R.**: Methodology, Validation, Formal analysis. **F.F.A.** and **C.P.S.:** Methodology, Validation, Visualization, Funding acquisition, Writing - Original Draft. **O.N.O.J., J.A.** and **E.L.:** Methodology, Validation, Data Curation, Visualization, Funding acquisition, Writing - Original Draft, Writing - Review & Editing.

Declaration of competing interest

The authors declare that they have no known competing financial interests or personal relationships that could have appeared to influence the work reported in this paper.

Data availability

Data will be made available on request.

Acknowledgments

J.A. acknowledges the Universitat Jaume I (project UJI-B2019-30) and the Ministerio de Ciencia, Innovación y Universidades (Spain) (project PGC2018094417-B-I00) for financially supporting this research. M.A. was supported by the Margarita Salas postdoctoral contract MGS/2021/21 (UP2021-021) financed by the European Union-NextGenerationEU. F.F.A. and J.M.A.R. were sponsored by PETROBRAS (Project No. 2017/00010-7). The authors would also like to thank the financial aid from the Fundação de Amparo à Pesquisa do Estado de São Paulo – FAPESP (2013/07296-2, 2016/13423-5, 2018/22214-6), the Financiadora de Estudos e Projetos – FINEP, the Coordenação de Aperfeiçoamento de Pessoal de Nível Superior – CAPES (Financial Code 001) and the Conselho Nacional de Desenvolvimento Científico e Tecnológico – CNPq (Grant no.141964/2018-9).

Appendix A. Supplementary data

Supplementary data to this article can be found online at https://doi.org/10.1016/j.bioadv.2022.213097.

References

[1] K.L. Wyres, M.M.C. Lam, K.E. Holt, Population genomics of Klebsiella pneumoniae, Nat. Rev. Microbiol. 18 (2020) 344–359, https://doi.org/10.1038/s41579-019-0315-1.

[2] C.Y. Effah, T. Sun, S. Liu, Y. Wu, Klebsiella pneumoniae: an increasing threat to public health, Ann. Clin. Microbiol. Antimicrob. 19 (2020) 1, https://doi.org/10.1186/s12941-019-0343-8.

[3] J.A. Bengoechea, J.S. Pessoa, Klebsiella pneumoniae infection biology: living to counteract host defences, FEMS Microbiol. Rev. 43 (2019) 123–144, https://doi.org/10.1093/femsre/fuy043.

[4] R.M. Martin, M.A. Bachman, Colonization, infection, and the accessory genome of Klebsiella pneumoniae, Front. Cell. Infect. Microbiol. 8 (2018) 4, https://doi.org/10.3389/fcimb.2018.00004.

[5] A. Tuñón-Molina, K. Takayama, E.M. Redwan, V.N. Uversky, J. Andrés, Á. Serrano-Aroca, Protective face masks: current status and future trends, ACS Appl. Mater. Interfaces 13 (2021) 56725–56751, https://doi.org/10.1021/acsami.1c12227.

[6] M. Assis, L.G.P. Simoes, G.C. Tremiliosi, L.K. Ribeiro, D. Coelho, D.T. Minozzi, R. I. Santos, D.C.B. Vilela, L.H. Mascaro, J. Andrés, E. Longo, PVC-SiO2-ag composite as a powerful biocide and anti-SARS-CoV-2 material, J. Polym. Res. 28 (2021) 361, https://doi.org/10.1007/s10965-021-02729-1.

[7] L.K. Ribeiro, M. Assis, L.R. Lima, D. Coelho, M.O. Gonçalves, R.S. Paiva, L. N. Moraes, L.F. Almeida, F. Lipsky, M.A. San-Miguel, L.H. Mascaro, R.M.T. Grotto, C.P. Sousa, I.L.V. Rosa, S.A. Cruz, J. Andrés, E. Longo, Bioactive Ag3PO4/Polypropylene composites for inactivation of SARS-CoV-2 and other important public health pathogens, J. Phys. Chem. B 125 (2021) 10866–10875, https://doi.org/10.1021/acs.jpcb.1c05225.

[8] M. Assis, L.G.P. Simoes, G.C. Tremiliosi, D. Coelho, D.T. Minozzi, R.I. Santos, D.C. B. Vilela, J.R. do Santos, L.K. Ribeiro, I.L.V. Rosa, L.H. Mascaro, J. Andrés, E. Longo, SiO2-Ag composite as a highly virucidal material: a roadmap that rapidly eliminates SARS-CoV-210.3390/nano11030638, Nanomaterials 11 (2021) 638.

[9] P.S. Lemos, G.S. Silva, R.A. Roca, M. Assis, R. Torres-Mendieta, H. Beltran-Mir, G. Minguez-Vega, E. Cordoncillo, J. Andrés, E. Longo, Laser and electron beam-induced formation of Ag/Cr structures on Ag2CrO4, Phys. Chem. Chem. Phys. 21 (2019) 6101–6111, https://doi.org/10.1039/C8CP07263A.

[10] M. Assis, T. Robeldo, C.C. Foggi, A.M. Kubo, G. Mínguez-Vega, E. Condoncillo, H. Beltran-Mir, R. Torres-Mendieta, J. Andrés, M. Oliva, C.E. Vergani, P. A. Barbugli, E.R. Camargo, R.C. Borra, E. Longo, Ag Nanoparticles/α-Ag2WO4 composite formed by electron beam and femtosecond irradiation as potent antifungal and antitumor agents, Sci. Rep. 9 (2019) 9927, https://doi.org/10.1038/s41598-019-46159-y.

[11] M. Assis, E. Cordoncillo, R. Torres-Mendieta, H. Beltrán-Mir, G. Mínguez-Vega, R. Oliveira, E.R. Leite, C.C. Foggi, C.E. Vergani, E. Longo, J. Andrés, Towards the scale-up of the formation of nanoparticles on α-Ag2WO4 with bactericidal properties by femtosecond laser irradiation, Sci. Rep. 8 (2018) 1–11, https://doi.org/10.1038/s41598-018-19270-9.

[12] M. Assis, C.C. de Foggi, V. Teodoro, J.P. de Campos, C.E. da Costa, T. Silva, P. F. Robeldo, C.E. Caperucci, R.C. Vergani, I. Borra, A.F. Sorribes, M.A. Gouveia, J. San-Miguel, E.Longo Andrés, Surface-dependent photocatalytic and biological activities of Ag2CrO4: integration of experiment and simulation, Appl. Surf. Sci. 545 (2021), 148964, https://doi.org/10.1016/j.apsusc.2021.148964.

[13] L.P. Oliveira, C.C. de Foggi, M. Assis, J. Andrés, E. Longo, C.E. Vergani, B.N.A.da S. Pimentel, Increasing the photocatalytic and fungicide activities of Ag3PO4 microcrystals under visible-light irradiation, Ceram. Int. 47 (2021) 22604–22614, https://doi.org/10.1016/j.ceramint.2021.04.272.

[14] C.C. De Foggi, R.C. De Oliveira, M. Assis, M.T. Fabbro, V.R. Mastelaro, C. E. Vergani, L. Gracia, J. Andrés, E. Longo, A.L. Machado, Unvealing the role of β-Ag2MoO4 microcrystals to the improvement of antibacterial activity, Mater. Sci. Eng. C. (2020), 110765, https://doi.org/10.1016/j.msec.2020.110765.

[15] R.C. de Oliveira, C.C. de Foggi, M.M. Teixeira, M.D.P. Silva, M. Assis, E. M. Francisco, B.N.A.S. Pimentel, C.E. Vergani, A.L. Machado, P.F.dos S. Pereira, J. Andres, L. Gracia, E. Longo, Mechanism of antibacterial activity via morphology change of α-AgVO3: theoretical and experimental insights, ACS Appl. Mater. Interfaces 9 (2017) 11472–11481, https://doi.org/10.1021/acsami.7b00920.

[16] T.R. Machado, N.G. Macedo, M. Assis, C. Donate-Buendia, G. Minguez-Vega, M. M. Teixeira, C.C. Foggi, C.E. Vergani, H. Beltran-Mir, J. Andrés, E. Cordoncillo, E. Longo, From complex inorganic oxides to Ag–Bi nanoalloy: synthesis by femtosecond laser irradiation, ACS Omega 3 (2018) 9880–9887, https://doi.org/10.1021/acsomega.8b01264.

[17] O. Monfort, P. Petrisková, Binary and ternary vanadium oxides: general overview, physical properties, and photochemical processes for environmental applications, in: Processes 9, 2021, p. 214, https://doi.org/10.3390/pr9020214.

[18] R.C. de Oliveira, L. Gracia, M. Assis, M.S. Li, J. Andres, E. Longo, L.S. Cavalcante, Disclosing the electronic structure and optical properties of Ag4V2O7 crystals: experimental and theoretical insights, CrystEngComm 18 (2016) 6483–6491, https://doi.org/10.1039/C6CE01269H.

[19] A. Beltrán, L. Gracia, J. Andrés, E. Longo, First-principles study on polymorphs of AgVO3: assessing to structural stabilities and pressure-induced transitions, J. Phys. Chem. C 121 (2017) 27624–27642, https://doi.org/10.1021/acs.jpcc.7b09865.

[20] R.C. Oliveira, M. Assis, M.M. Teixeira, M.D.P. Silva, M.S. Li, J. Andres, L. Gracia, E. Longo, An experimental and computational study of β-AgVO3: optical properties and formation of Ag nanoparticles, J. Phys. Chem. C 120 (2016) 12254–12264, https://doi.org/10.1021/acs.jpcc.6b02840.

[21] A.P.M. Monteiro, R.D. Holtz, L.C. Fonseca, C.H.Z. Martins, M. Sousa, L.A.V. Luna, D.L.S. Maia, O.L. Alves, Nano silver vanadate AgVO3: synthesis, new functionalities and applications, Chem. Rec. 18 (2018) 973–985, https://doi.org/10.1002/tcr.201700086.

[22] S. Kreve, V.C. Oliveira, L. Bachmann, O.L. Alves, A.C.Dos Reis, Influence of AgVO3 incorporation on antimicrobial properties, hardness, roughness and adhesion of a soft denture liner, Sci. Rep. 9 (2019), 11889, https://doi.org/10.1038/s41598-019-48228-8.

[23] Z. Xiang, Y. Wang, Z. Yang, D. Zhang, Heterojunctions of β-AgVO3/BiVO4 composites for enhanced visible-light-driven photocatalytic antibacterial activity, J. Alloys Compd. 776 (2019) 266–275, https://doi.org/10.1016/j.jallcom.2018.10.287.

[24] J. Zhang, J. Wang, H. Xu, X. Lv, Y. Zeng, J. Duan, B. Hou, The effective photocatalysis and antibacterial properties of AgBr/AgVO3 composites under visible-light, RSC Adv. 9 (2019) 37109–37118, https://doi.org/10.1039/C9RA06810D.

[25] M. Pudukudy, Q. Jia, H. Wang, S. Shan, R. Rajendran, Influence of synthesis parameters on the crystalline, structural, textural, optical and photocatalytic properties of α and β polymorphs of AgVO3 nanorods, Mater. Sci. Semicond. Process. 107 (2020), 104824, https://doi.org/10.1016/j.mssp.2019.104824.

[26] A. Singh, D.P. Dutta, A. Ballal, A.K. Tyagi, M.H. Fulekar, Visible light driven photocatalysis and antibacterial activity of AgVO3 and Ag/AgVO3 nanowires, Mater. Res. Bull. 51 (2014) 447–454, https://doi.org/10.1016/j.materresbull.2014.01.001.

[27] L. Liu, W. Dai, H. Zhu, Y. Gu, K. Wang, C. Li, C. Pan, M. Zhou, J. Liu, Artificial cathode-electrolyte interphase towards high-performance lithium-ion batteries: a case study of β-AgVO3, Nanomaterials. 11 (2021) 569, https://doi.org/10.3390/nano11030569.

[28] D. McNulty, Q. Ramasse, C. O'Dwyer, The structural conversion from α-AgVO3 to β-AgVO3: ag nanoparticle decorated nanowires with application as cathode materials for li-ion batteries, Nanoscale 8 (2016) 16266–16275, https://doi.org/10.1039/C6NR04825K.

[29] L. Mai, L. Xu, Q. Gao, C. Han, B. Hu, Y. Pi, Single β-AgVO3 nanowire H2S sensor, Nano Lett. 10 (2010) 2604–2608, https://doi.org/10.1021/nl1013184.

[30] J.S. da Silva, T.R. Machado, A.B. Trench, A.D. Silva, V. Teodoro, P.C. Vieira, T. A. Martins, E. Longo, Enhanced photocatalytic and antifungal activity of hydroxyapatite/α-AgVO3 composites, Mater. Chem. Phys. 252 (2020), 123294, https://doi.org/10.1016/j.matchemphys.2020.123294.

[31] R.D. Holtz, A.G. Souza Filho, M. Brocchi, D. Martins, N. Durán, O.L. Alves, Development of nanostructured silver vanadates decorated with silver nanoparticles as a novel antibacterial agent, Nanotechnology 21 (2010), 185102, https://doi.org/10.1088/0957-4484/21/18/185102.

[32] R. Fernández de Luis, A. Martínez-Amesti, E.S. Larrea, L. Lezama, A.T. Aguayo, M. I. Arriortua, Composite β-AgVO3@V1.65+V0.44+O4.8 hydrogels and xerogels for iodide capture, J. Mater. Chem. A 3 (2015) 19996–20012, https://doi.org/10.1039/C5TA04189A.

[33] J.S. Silva, T.R. Machado, T.A. Martins, M. Assis, C.C. Foggi, N.G. Macedo, H. Beltrán-Mir, E. Cordoncillo, J. Andrés, E. Longo, α-AgVO3 decorated by hydroxyapatite (Ca10(PO4)6(OH)2): tuning its photoluminescence emissions and bactericidal activity, Inorg. Chem. 58 (2019) 5900–5913, https://doi.org/10.1021/acs.inorgchem.9b00249.

[34] B.N.A.S. Pimentel, F.H. Marin-Dett, M. Assis, P.A. Barbugli, E. Longo, C.E. Vergani, Antifungal activity and biocompatibility of α-AgVO3, α-Ag2WO4, and β-Ag2MoO4 using a three-dimensional coculture model of the oral mucosa, Front. BioengBiotechnol. 10 (2022) 1–14, https://doi.org/10.3389/fbioe.2022.826123.

[35] D. Zhou, Y.-Y. Wang, F.-R. Wang, J.-K. Liu, X.-M. Zhang, Design and application of Ag3PO4 @Ag4V2O7 Z-scheme photocatalysts with a micro-Nano tube-cluster structure for the co-degradation of nitrate and ammonia in wastewater, Ind. Eng. Chem. Res. 58 (2019) 18027–18035, https://doi.org/10.1021/acs.iecr.9b03623.

[36] J. Wang, J. Chen, Y. Yu, W. Yu, X. Meng, J. Chen, D. Li, One-step SDS-assisted hydrothermal synthesis and photoelectrochemical study of Ag4V2O7 nanorods decorated with Ag nanoparticles, CrystEngComm 17 (2015) 6661–6668, https://doi.org/10.1039/C5CE01134E.
[37] C. Ren, J. Fan, S. Liu, W. Li, F. Wang, H. Li, X. Liu, Z. Chang, One-step hydrothermal synthesis of novel Ag3VO4/Ag4V2O7 composites for enhancing visible-light photocatalytic performance, RSC Adv. 6 (2016) 95156–95164, https://doi.org/10.1039/C6RA22150E.
[38] G. Wang, W. Jin, A.M. Qasim, A. Gao, X. Peng, W. Li, H. Feng, P.K. Chu, Antibacterial effects of titanium embedded with silver nanoparticles based on electron-transfer-induced reactive oxygen species, Biomaterials 124 (2017) 25–34, https://doi.org/10.1016/j.biomaterials.2017.01.028.
[39] D.T. Castro, M.L.da C.P.F. Valente, C.P. Aires, O.L. Alves, A.C. Reis, Elemental ion release and cytotoxicity of antimicrobial acrylic resins incorporated with nanomaterial, Gerodontology 34 (2017) 320–325, https://doi.org/10.1111/ger.12267.
[40] A.B.V. Teixeira, N.C.S. Moreira, C.S. Takahashi, M.A. Schiavon, O.L. Alves, A. C. Reis, Cytotoxic and genotoxic effects in human gingival fibroblast and ions release of endodontic sealers incorporated with nanostructured silver vanadate, J. Biomed. Mater. Res. Part B Appl. Biomater. 109 (2021) 1380–1388, https://doi.org/10.1002/jbm.b.34798.
[41] M.C. Artal, R.D. Holtz, F. Kummrow, O.L. Alves, G.de A. Umbuzeiro, The role of silver and vanadium release in the toxicity of silver vanadate nanowires toward Daphnia similis, Environ. Toxicol. Chem. 32 (2013) 908–912, https://doi.org/10.1002/etc.2128.
[42] B.N.A.S. Pimentel, C.C. de Foggi, P.A. Barbugli, R.C. de Oliveira, E.D. de Avila, E. Longo, C.E. Vergani, Antifungal activity and biocompatibility of α-AgVO3 microcrystals: a promising material against oral Candida disease, Mater. Sci. Eng. C. 108 (2020), 110405, https://doi.org/10.1016/j.msec.2019.110405.
[43] Y. Wang, Y. Zeng, X. Chen, Q. Wang, L. Guo, S. Zhang, Q. Zhong, One-step hydrothermal synthesis of a novel 3D BiFeWOx/Bi2WO6 composite with superior visible-light photocatalytic activity, Green Chem. 20 (2018) 3014–3023, https://doi.org/10.1039/C7GC03731G.
[44] Q. Wang, X. Zhou, S. Ji, S. Li, J. Gu, L. Shen, P. Liu, J. Yin, G. Xu, W. Shi, Synthesis and photocatalysis of novel Z-scheme CeO2/Ag-AgVO3 heterojunction nanofibers and their efficient antibacterial properties, J. Environ. Chem. Eng. 9 (2021), 106498, https://doi.org/10.1016/j.jece.2021.106498.
[45] R.C. Oliveira, M.M. Teixeira, J.P.C. Costa, M. Penha, E.M. Francisco, J.S. da Silva, M.S. Li, E. Longo, L. Gracia, J. Andrés, α- and β-AgVO3 polymorphs as photoluminescent materials: an example of temperature-driven synthesis, Ceram. Int. 44 (2018) 5939–5944, https://doi.org/10.1016/j.ceramint.2017.12.161.
[46] I. Karaiskos, H. Giamarellou, Carbapenem-sparing strategies for ESBL producers: when and how, Antibiotics 9 (2020) 61, https://doi.org/10.3390/antibiotics9020061.
[47] M. Bassetti, M. Peghin, How to manage KPC infections, Ther. Adv. Infect. Dis. 7 (2020), 2049936120912049, https://doi.org/10.1177/2049936120912049.
[48] T. Mosmann, Rapid colorimetric assay for cellular growth and survival: application to proliferation and cytotoxicity assays, J. Immunol. Methods 65 (1983) 55–63, https://doi.org/10.1016/0022-1759(83)90303-4.
[49] G. Repetto, A. del Peso, J.L. Zurita, Neutral red uptake assay for the estimation of cell viability/cytotoxicity, Nat. Protoc. 3 (2008) 1125–1131, https://doi.org/10.1038/nprot.2008.75.
[50] B.E. Saltzman, Colorimetric microdetermination of nitrogen dioxide in atmosphere, Anal. Chem. 26 (1954) 1949–1955, https://doi.org/10.1021/ac60096a025.
[51] L.C. Green, D.A. Wagner, J. Glogowski, P.L. Skipper, J.S. Wishnok, S. R. Tannenbaum, Analysis of nitrate, nitrite, and nitrate in biological fluids, Anal. Biochem. 126 (1982) 131–138, https://doi.org/10.1016/0003-2697(82)90118-X.
[52] A.R. Dória, M. Pupo, G.O.S. Santos, D.S. Vilar, N.H. Torres, L.F.R. Ferreira, E. B. Cavalcanti, K.I.B. Eguiluz, G.R. Salazar-Banda, Electrochemical oxidation of indanthrene blue dye in a filter-press flow reactor and toxicity analyses with raphidocelis subcapitata and Lactuca sativa, Ecotoxicol. Environ. Saf. 198 (2020), 110659, https://doi.org/10.1016/j.ecoenv.2020.110659.
[53] W. Wang, Root elongation method for toxicity testing of organic and inorganic pollutants, Environ. Toxicol. Chem. 6 (1987) 409–414, https://doi.org/10.1002/etc.5620060509.
[54] M. Herraiz-Carboné, E. Lacasa, S. Cotillas, M. Vasileva, P. Cañizares, M.A. Rodrigo, C. Sáez, The role of chloramines on the electrodisinfection of Klebsiella pneumoniae in hospital urines, Chem. Eng. J. 409 (2021), 128253, https://doi.org/10.1016/j.cej.2020.128253.
[55] M.C.V.M. Starling, R.P. Mendonça Neto, G.F.F. Pires, P.B. Vilela, C.C. Amorim, Combat of antimicrobial resistance in municipal wastewater treatment plant effluent via solar advanced oxidation processes: achievements and perspectives, Sci. Total Environ. 786 (2021), 147448, https://doi.org/10.1016/j.scitotenv.2021.147448.
[56] V.L. Prasanna, R. Vijayaraghavan, Insight into the mechanism of antibacterial activity of ZnO: surface defects mediated reactive oxygen species even in the dark, Langmuir 31 (2015) 9155–9162, https://doi.org/10.1021/acs.langmuir.5b02266.
[57] S. Podder, S. Halder, A. Roychowdhury, D. Das, C.K. Ghosh, Superb hydroxyl radical-mediated biocidal effect induced antibacterial activity of tuned ZnO/chitosan type II heterostructure under dark, J. Nanopart. Res. 18 (2016) 294, https://doi.org/10.1007/s11051-016-3605-9.
[58] T.R. Mosmann, R.L. Coffman, Two types of mouse helper T-cell clone: implications for immune regulation, Immunol. Today 8 (1987) 223–227, https://doi.org/10.1016/0167-5699(87)90171-X.
[59] M.J. Stoddart, Mammalian cell viability: methods and protocols - cell viability assays, Methods Mol. Biol. 740 (2011) 1–6, https://doi.org/10.1007/978-1-61779-108-6.
[60] A.B.V. Teixeira, D.T. Castro, M.A. Schiavon, A.C. dos Reis, Cytotoxicity and release ions of endodontic sealers incorporated with a silver and vanadium base nanomaterial, Odontology 108 (2020) 661–668, https://doi.org/10.1007/s10266-020-00507-x.
[61] R.P. Singh, M. Das, V. Thakare, S. Jain, Functionalization density dependent toxicity of oxidized multiwalled carbon nanotubes in a murine macrophage cell line, Chem. Res. Toxicol. 25 (2012) 2127–2137, https://doi.org/10.1021/tx300228d.
[62] A. Almeida, S. Moncada, J.P. Bolaños, Nitric oxide switches on glycolysis through the AMP protein kinase and 6-phosphofructo-2-kinase pathway, Nat. Cell Biol. 6 (2004) 45–51, https://doi.org/10.1038/ncb1080.
[63] A. Tauffenberger, P.J. Magistretti, Reactive oxygen species: beyond their reactive behavior, Neurochem. Res. 46 (2021) 77–87, https://doi.org/10.1007/s11064-020-03208-7.
[64] S. Basuroy, D. Tcheranova, S. Bhattacharya, C.W. Leffler, H. Parfenova, Nox4 NADPH oxidase-derived reactive oxygen species, via endogenous carbon monoxide, promote survival of brain endothelial cells during TNF-α-induced apoptosis, Am. J. Physiol. Cell Physiol. 300 (2011), C256-65, https://doi.org/10.1152/ajpcell.00272.2010.
[65] A.V. Snezhkina, A.V. Kudryavtseva, O.L. Kardymon, M.V. Savvateeva, N. V. Melnikova, G.S. Krasnov, A.A. Dmitriev, ROS generation and antioxidant defense systems in normal and malignant cells, Oxid. Med. Cell. Longev. 2019 (2019), https://doi.org/10.1155/2019/6175804, 6175804.
[66] C. Suriyasak, K. Harano, K. Tanamachi, K. Matsuo, A. Tamada, M. Iwaya-Inoue, Y. Ishibashi, Reactive oxygen species induced by heat stress during grain filling of rice (Oryza sativa L.) are involved in occurrence of grain chalkiness, J. Plant Physiol. 216 (2017) 52–57, https://doi.org/10.1016/j.jplph.2017.05.015.
[67] X. Yang, F. Zhang, M. Yang, Y. He, Z. Li, J. Yang, X. Wang, The NADPH-oxidase LsRbohC1 plays a role in lettuce (Lactuca sativa) seed germination, Plant Physiol. Biochem. 154 (2020) 751–757, https://doi.org/10.1016/j.plaphy.2020.05.042.
[68] N.W. Lepp, The effect of vanadium on germination and seedling growth of lettuce (Lactuca sativa L. C. VSalad Bowi), Zeitschrift Für Pflanzenphysiologie 83 (1977) 185–188, https://doi.org/10.1016/S0044-328X(77)80072-X.
[69] F. Mirzajani, H. Askari, S. Hamzelou, M. Farzaneh, A. Ghassempour, Effect of silver nanoparticles on Oryza sativa L. and its rhizosphere bacteria, Ecotoxicol. Environ. Saf. 88 (2013) 48–54, https://doi.org/10.1016/j.ecoenv.2012.10.018.
[70] P. Kubelka, Ein Beitrag zur Optik der Farbanstriche, Zeitschrift Fur Tech. Phys. 12 (1931) 593–601.
[71] K. Rajeshwar, A. Vali, Phase pure silver pyrovanadate (Ag4V2O7) thin films: synthesis via a hybrid cathodic/anodic approach and characterization, in: ECS Meet. Abstr. MA2021-02, 2021, https://doi.org/10.1149/MA2021-0213645mtgabs, 645–645.
[72] C.-M. Huang, G.-T. Pan, Y.-C.M. Li, M.-H. Li, T.C.-K. Yang, Crystalline phases and photocatalytic activities of hydrothermal synthesis Ag3VO4 and Ag4V2O7 under visible light irradiation, Appl. Catal. A Gen. 358 (2009) 164–172, https://doi.org/10.1016/j.apcata.2009.02.007.
[73] Q. Xie, Z. Xu, B. Hu, X. He, L. Zhu, Preparation of a novel silk microfiber covered by AgCl nanoparticles with antimicrobial activity, Microsc. Res. Tech. 80 (2017) 272–279, https://doi.org/10.1002/jemt.22683.
[74] S. San Martín, M.J. Rivero, I. Ortiz, Unravelling the mechanisms that drive the performance of photocatalytic hydrogen production, Catalysts 10 (2020) 901, https://doi.org/10.3390/catal10080901.
[75] D.L. Wood, J. Tauc, Weak absorption tails in amorphous semiconductors, Phys. Rev. B 5 (1972) 3144–3151, https://doi.org/10.1103/PhysRevB.5.3144.
[76] A.M. Pisoschi, A. Pop, F. Iordache, L. Stanca, G. Predoi, A.I. Serban, Oxidative stress mitigation by antioxidants - an overview on their chemistry and influences on health status, Eur. J. Med. Chem. 209 (2021), 112891, https://doi.org/10.1016/j.ejmech.2020.112891.
[77] M. Shaaban, A.M. El-Mahdy, Biosynthesis of ag, se, and ZnO nanoparticles with antimicrobial activities against resistant pathogens using waste isolate streptomyces enissocaesilis, IET Nanobiotechnol. 12 (2018) 741–747, https://doi.org/10.1049/iet-nbt.2017.0213.
[78] K.I. Alsamhary, Eco-friendly synthesis of silver nanoparticles by Bacillus subtilis and their antibacterial activity, saudiJ. Biol. Sci. 27 (2020) 2185–2191, https://doi.org/10.1016/j.sjbs.2020.04.026.
[79] W. Klöckner, C.P. Vidal, C.L. de Dicastillo, R.M. Yadav, D.P. Singh, Large scale synthesis of silver vanadate nanowires consolidated into bulk cylinder with enhanced antibacterial properties, Mater. Lett. 278 (2020), 128403, https://doi.org/10.1016/j.matlet.2020.128403.